Memristive Control of Plasmon-Mediated Nonlinear Photoluminescence in Au Nanowires

Deepak K Sharma, Adrian Agreda, Florian Dell'ova, Konstantin Malchow, Gérard Colas des Francs, Erik Dujardin, Alexandre Bouhelier

Memristive control of plasmon-mediated nonlinear photoluminescence in Au nanowires

Deepak K. Sharma,[†,‡] Adrian Agreda,[†,¶] Florian Dell'Ova,[†] Konstantin Malchow,[†,§] Gérard Colas des Francs,[†] Erik Dujardin,[†] and Alexandre Bouhelier[*,†]

†*Laboratoire Interdisciplinaire Carnot de Bourgogne, UMR 6303 CNRS, Université de Bourgogne, 9 Avenue Alain Savary, 21000 Dijon, France*

‡*Current address: Institute of Materials Research and Engineering (IMRE), Agency for Science, Technology and Research (A*STAR), 2 Fusionopolis Way, Innovis # 08-03, Singapore 138634, Republic of Singapore*

¶*Current address: ELORPrintTec, Allée Geoffroy Saint-Hilaire, F-33600 Pessac, France*

§*Current address: Laboratory of Quantum Nano Optics, EPFL Lausanne, 1015 Lausanne, Switzerland*

E-mail: alexandre.bouhelier@u-bourgogne.fr

Abstract

Nonlinear photoluminescence (N-PL) is a broadband photon emission arising from a non-equilibrium heated electron distribution generated at the surface of metallic nanostructures by an ultrafast pulsed laser illumination. N-PL is sensitive to surface morphology, local electromagnetic field strength, and electronic band structure making it relevant to probe optically excited nanoscale plasmonic systems. It also has been key to access the complex multiscale time dynamics ruling electron thermalization. Here, we show that the plasmon-mediated N-PL emitted by a gold nanowire can be modified by an electrical architecture featuring a nanogap. Upon voltage activation, we observe that

N-PL becomes dependent to the electrical transport dynamics and can thus be locally modulated. This finding brings an electrical leverage to externally control the photoluminescence generated from metal nanostructures, and constitutes an asset for the development of emerging nanoscale interface devices managing photons and electrons.

Keywords

Metal luminescence, Hot electrons, Plasmonic nanowire, Memristive devices, Memristor

Introduction

The illumination of metallic nanostructures by ultrashort laser pulses at near-IR wavelengths induces a broadband up-converted emission spanning the visible spectral regime. Under high-intensity femtosecond excitation, this nonlinear signal has been shown to be dominated by a thermal luminescence continuum emitted by out-of-equilibrium surface electrons with transiently elevated temperatures.[1–6] Indeed, following the absorption of the light pulse, the temperature of the electron gas at the surface of the metal can reach thousands of Kelvins for about a picosecond[6,7] and radiates before equilibrating with the phonons.[8–10] This nonlinear photoluminescence (N-PL) has been studied on a wide range of plasmonic geometries and materials.[3,11–18]An important feature is the dramatic signal enhancement observed from hot-spots favored by the presence of localized resonances (e.g. at nanoparticles[19,20]). Such local signal enhancements are observed because the luminescence emanates from hot thermal electrons generated at the surface of the metal.[6,21,22] Further, in structures sustaining surface plasmon propagation (e.g. nanowires, cavities), N-PL has been shown to be spatially distributed throughout the modal landscape.[22,23] Hence, N-PL has been a key observable to unlock ultrafast light-matter interactions, and this response found numerous usages. For instance, it has been used as a luminescent marker in bioimaging,[24,25] or as an observable to develop plasmonic logic gates.[26]

The sensitivity of the N-PL to surface electrons and morphology motivates a closer examination of the signal in the presence of intricate field-driven surface effects involving atomic-scale dynamics and charge transport. These nuances serve as crucial elements for advancing the next generation of nanoscale devices in applications including energy harvesting,[27] computing and memory components,[28,29] tunable metasurfaces,[30] and beyond.

In this study, we show that N-PL, spatially distributed by a propagating surface plasmon in a Au nanowire (AuNW), can be locally sensitive to tiny conductance changes and atomic-scale restructuration of a nanogap. Under the application of electrostatic bias pulses across the nanogap, we observe a progressive evolution of the plasmon-mediated N-PL that eventually leads to a drastic voltage-driven modulation of its intensity. We establish that the light emission directly translates the electronic dynamics and atomic-scale movements within the nanogap.

Results and discussion

System description

Figure 1(a) is a scanning electron microscopy (SEM) image of a typical AuNW and the in-plane electrode architecture. The fabrication process involves standard electron beam lithography patterning of small features (the nanowire and electrode shown in SEM image) and photolithography patterning of extended microelectrodes (not shown in SEM image) followed by thin film deposition (1 nm Cr, $\sim$ 90 nm Au) on a standard glass coverslip (see Methods for detailed information on device fabrication).[22,31] The AuNW system is then encapsulated in a polymer layer (Poly(methyl methacrylate) - PMMA, thickness $\sim$ 200 nm). The PMMA acts as a protective layer against atmospheric contaminants. The nanowires used in our experiments have cross-section of approximately $\sim$ 180 nm in width, $\sim$ 90 nm in thickness, and they support a bound surface plasmon mode which propagates at the excitation wavelength.[32] The laser is tuned at 810 nm wavelength and emits 140 fs pulse

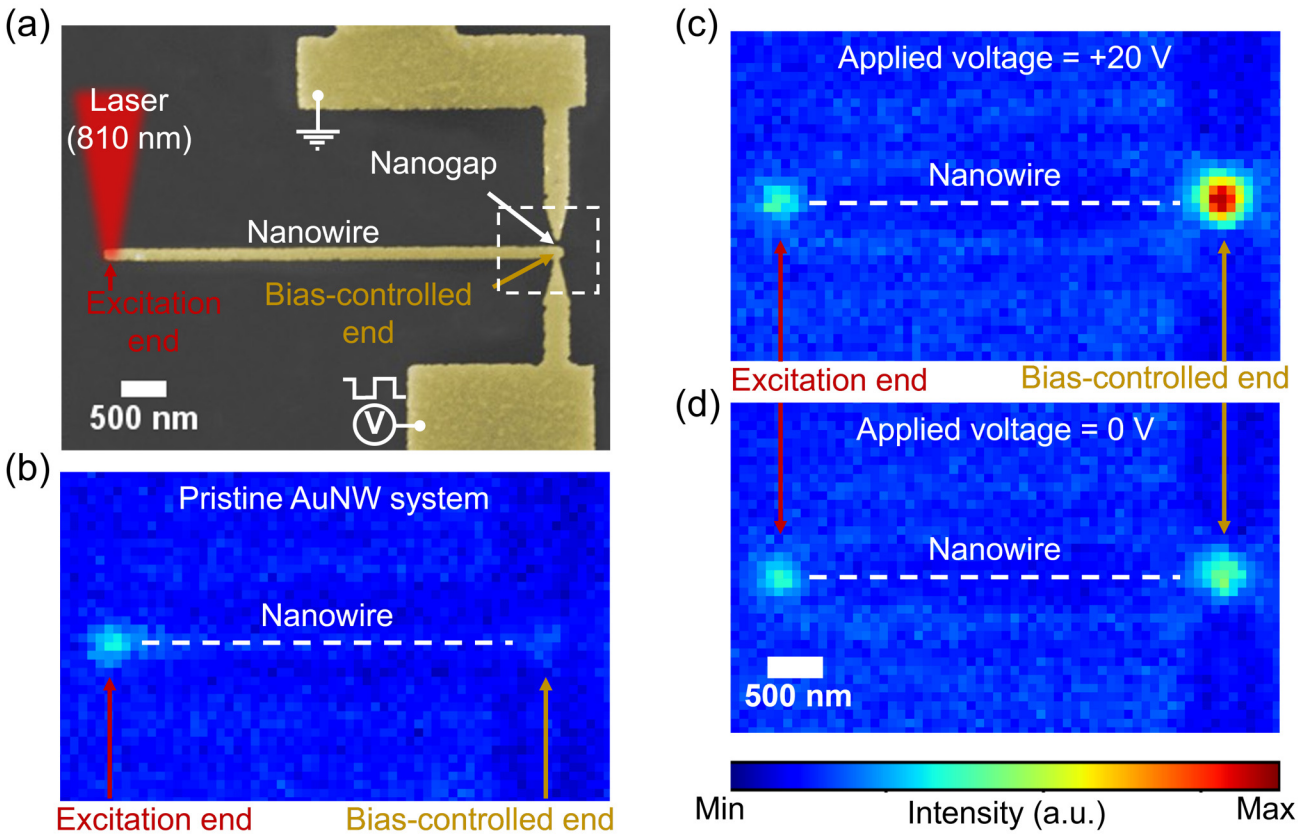

Figure 1: Overview of the AuNW system and its operation: (a) The device configuration seen from a colorized SEM image of a typical AuNW system. A tightly focused laser excitation at the left end of the AuNW is used to launch a propagating surface plasmon at the pump wavelength (810 nm). The distal end is electrostatically controlled by a tapered electrode placed at 50 nm distance from the AuNW surface. (b) Spatial distribution of the N-PL on a pristine AuNW. The signal arises from the extremity directly excited by the focused laser as well as from the distal end via the mediation of a surface plasmon.(c) and (d) Same as in (b) for $V = 20$ V and $V = 0$ V respectively after electrical activation of the nanogap. A localized enhancement of the signal at the bias-controlled end is readily seen with applied bias. A dashed white line guides the long axis of the nanowire.

at a 80 MHz repetition rate. The surface plasmon is launched by edge scattering when the laser is focused to the left extremity of the AuNW.[33] Focusing is achieved with the help of a high numerical aperture (N.A.) objective (N.A. = 1.49). The electrical potential of the AuNW is applied via a first tapered electrode electrically connected to its extremity. A second tapered Au electrode acting as a ground is adjacent to it with a gap of tens of nanometers. Figure S1 in the Supporting Information presents the details of the optical and electrical measurements.

Figure 1(b) is a wide-field optical image of the N-PL distribution captured by a charge-coupled device (CCD) when the AuNW is excited at its left end before any bias application. The estimated optical peak intensity at the focus is ~ 7.5 GW/m^2. The laser and the second harmonic generated by the Au surface are rejected from the image using spectral filtering. A low-intensity halogen lamp illuminates the sample during the image acquisition in order to visually recognize the footprint of the system (dashed line representing the nanowire). The image shows a clear N-PL response from the excitation extremity where the laser intensity is focused, and a second weaker emission region located at the right end of the AuNW, near the nanogap. Here, the nanogap is about 50 nm wide and this AuNW extremity is referred to as the bias-controlled end. The relative N-PL intensities between the excitation extremity and bias-controlled end depend on the coupling factor to the plasmon mode, the length of the nanowire, and the geometry of the end-face. The N-PL emitted at the bias-controlled end is produced by end-face scattering of the surface plasmon traveling in the nanowire at the pump laser wavelength.[22] The N-PL spectrum emitted from there and in absence of a bias is presented in Figure S2 (Supporting Information). The spectrum features a blackbody-like tail confirming that with the laser intensity used here, N-PL reflects a spontaneous emission of thermal electrons.[5,6] An estimation of the temperature of the electronic distribution is inferred from a fit of the spectrum (Figure S2, Supporting Information) using Planck's law.[4,31,34] We find an electron temperature at the bias-controlled end to be $T_e = 1250$ K. This is a temperature somewhat cooler than previously reported values obtained from spec-

tra measured directly under the laser focus.[4,31] However, this is expected because the N-PL at the bias-controlled end is remotely generated from the laser focus through the mediation of a lossy surface plasmon propagating on the nanowire.

The situation changes when an electrostatic stress is applied between the nanowire and the ground electrode. Figure 1(c) shows the N-PL distribution when $V = +20$ V. A ~ 100 % enhancement of the N-PL signal is observed at the bias-controlled end compared to the no-bias condition displayed in Figure 1(d). Note that the N-PL intensity at the controlled end in Fig. 1(d) is significantly higher than in Fig. 1(b), although $V = 0$ V in both images. The change of the N-PL signal at the nanowire extremity is not immediately observed on a pristine system, but appears after a repeated electrical stress applied to the nanogap. The modulation of the plasmon-generated N-PL is visualized in real-time in the Supplementary Movie (M1, Supporting Information) when square electrostatic pulses (+20 V amplitude, 0.5 Hz frequency) are applied. In the upcoming sections, we delve into this activation process and explore how a voltage-driven dynamics influences the N-PL at the bias-controlled end.

Electrical activation of the nanogap

We initiate the activation process with a $V = +2$ V positive electrostatic bias pulse sequence applied to the pristine Au nanogap. We incrementally increase the voltage for subsequent pulse sequences. Throughout this activation process, we simultaneously record both the N-PL emission rate, and the second-harmonic generation (SHG) emitted from the bias-controlled end (area indicated by the white dashed rectangle in Figure 1(a)), as well as the electric current, I_{g}, flowing through the nanogap. Both N-PL and SHG are measured with the help of avalanche photodiode counting modules and are expressed in kct/s. Like the N-PL response, the SHG emitted from the nanowire end is produced by the plasmon propagating at the pump wavelength.[23] Because SHG is sensitive to minute changes of the nanowire surface,[35,36] we utilize SHG as a probe to monitor the structural integrity of the termination. At the beginning of the stress sequence, there is no measurable I_{g} crossing the

50 nm-wide gap.

In Figure 2, we provide a series of time series illustrating the evolution of these quantities as we apply square electrostatic bias pulses with a frequency of 0.5 Hz to the nanogap on the same device. The series displayed in Figure 2(a) starts with a pulse sequence at $V = +2$ V followed by one at $V = +3$ V. I_g remains barely above noise level (< 1 pA) and is mostly dominated by artefactual capacitive effect picked up during the leading and trailing edges of the pulse. During this pulse sequence, the N-PL and SHG signals are steady and remain unaffected by the bias. The SHG emitted at the distal end of the nanowire is here much weaker than N-PL emitted at the same location. In this sequence, SHG is buried in the dark noise of the detector (approximately 500 ct/s). Figure 2(b) is a time series acquired later and after repeated stress sequences done with increasing amplitudes (steps of $V = +1$ V). Here the series starts with $V = +5$ V. A modulated I_g is now clearly measured with an amplitude fluctuating during the pulse sequence.

This sequence is featuring a small but correlative modulation of the N-PL at each voltage pulse (see left inset). However, the baseline signal, measured at $V = 0$ V, is erratically evolving with time. It has increased from $\sim$ 10 kct/s at the onset of bias application at $t = 0$ s to $\sim$ 150 kct/s around $t = 850$ s under unchanged optical illumination conditions. Because N-PL is sensitive to the surface defects,[37] this close to 15-fold fluctuation of the baseline underscores bias-induced morphological changes occurring in the AuNW system. This restructuring of the nanowire termination is also confirmed by the SHG signal where the main N-PL changes are also registered (e.g. at $t = 710$ s, 740 s, 750 s and 810 s). Despite this reshaping of the system during the sequence affecting the overall response, the small superimposed modulation of the N-PL with the bias pulses remains observable over the entire frame.

The situation differs in the timelines represented in Figure 2(c) obtained after a prolonged application of positive pulse sequences. Both the N-PL and SHG baselines are now constant over the entire time trace suggesting that transient field-driven irreversible surface alteration

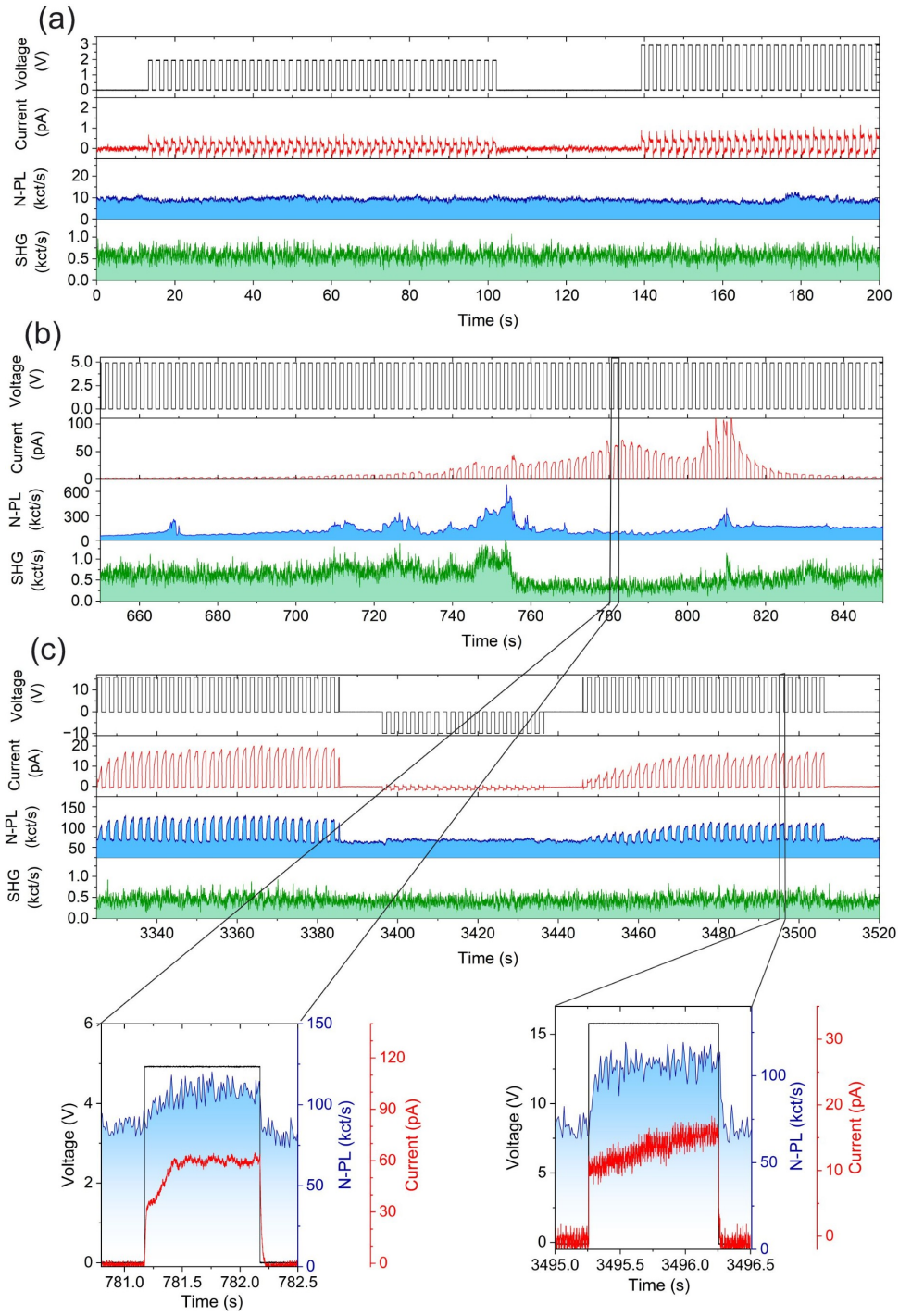

Figure 2: (a-c) Snapshots of the time series showing the evolution of modulation amplitudes in spatially filtered nonlinear photoluminescence (N-PL) and second-harmonic generation (SHG) from the bias-controlled end of AuNW and electric current, I_g passing through the nanogap under electrostatic bias pulse sequences. Single-pulse details of the time traces are shown at the bottom.

of the system is no longer occurring after the activation phase. In the steady regime, a ∼18 pA current flowing through the device is measured at each voltage pulse. This is accompanied by a clear modulation of the N-PL between ∼ 75 kct/s at $V = 0$ V to ∼ 120kct/s at $V = +16$ V, corresponding to a stable 60 % enhancement of the signal. The SHG also features a very small gain when the bias is applied, an effect already seen in our previous report.[31] In this earlier work, we demonstrated that N-PL intensity increases with the local electron gas temperature (T_e).[31] Dwelving on the fact that T_e varies as the inverse square root of the surface electron density, N_e, a capacitive accumulation of positive charges at the surface of the nanowire explains the signal enhancement upon application of positive bias pulses.[31] Figure S2 (Supporting Information) displays N-PL spectra taken at different voltages and the inferred electron temperature deduced from a fitting of the data with Planck's law. For $V = +14$ V, we find $T_e = 1292$ K, a raise of 42 K with respect to no bias condition. For $V = +20$ V, T_e reaches 1373 K confirming that a positive potential with respect to the ground electrode contributes to elevate the electron temperature via a capacitive change of N_e.

Figure 2(c) features an intriguing behavior when the voltage polarity of the pulses is reversed at $t = 3396$ s. Under pulses of amplitude $V = -10$ V, I_g changes its polarity, but its amplitude is significantly reduced, and the N-PL is no longer affected by the bias. This outcome is contrary to expectations. Indeed, keeping the capacitive scenario in mind, this polarity should lead to a periodic quenching of N-PL because of the higher electron density generated at the surface of the nanowire.[31] At $t = 3446$ s, +16 V voltage pulses are again applied to the system. The progressive buildup of the I_g amplitude over the first few pulses is concomitant to a clear restoration of the N-PL modulation. These initial observations imply the existence of additional factors influencing the electrostatic bias control of the N-PL, arguably stemming from intrinsic conduction dynamics within the nanogap, which we explore in the sections below.

Effect of conduction dynamics on nonlinear photoluminescence modulation

The modulation amplitude (calculated as the difference between the average signal level during a bias pulse and the average baseline signal between consecutive bias pulses) of I_g and the N-PL are clearly correlated. This is demonstrated in Figure 3(a) where the modulation amplitudes inferred from Figure 2(c) are plotted against each other for the two time windows corresponding to positive pulses sequences. A linear relationship is distinctly visible indicating that the same effect rules the two responses. The underlying mechanism is also dictating the time dynamics of the signals. From Figure 2(c), it is clear that the maximum modulation amplitudes for both I_g and the N-PL signals are not instantaneous but are reached after the application of a few voltage pulses. This progressive build-up of the modulation is even slower after applying the sequence of negative pulses. A comparison of the N-PL and I_g modulation amplitudes with the number of bias pulses is presented in Figure 3(b). We fit the data using an empirical charging function of the form $S = a(1 - \exp(-\mathrm{N}/\tau)) + \mathrm{c}$, where N is the number of pulses, and S is either I_g or the N-PL modulation amplitude, a is a weighting factor, τ is the characteristic growth coefficient and c accounts for residual offset of the experiment. a, τ and c are free parameters of the fit. The results (solid lines in Figure 3(b)) show that it takes between $N = 3$ to $N = 4$ pulses to reach maximum I_g modulation while 2 pulses are enough to attain the largest N-PL modulation during the first sequence of positive bias pulses. These figures are increased to 7 and 8 pulses of positive pulses (second sequence) respectively after negative pulses have been applied. Such behavior unambiguously underlines the occurrence of a volatile build-up of the conditions leading to a stable modulation.

To get more insight into the intrapulse dynamics, we have averaged the I_g and N-PL over many pulses showing a stable modulation. Figure 3(c) reveals that after the leading bias edge, I_g suddenly sets to about 11 pA and evolves with a gradual increase over hundreds of ms. The flow of electrical charges is an unambiguous marker of the formation of conductive

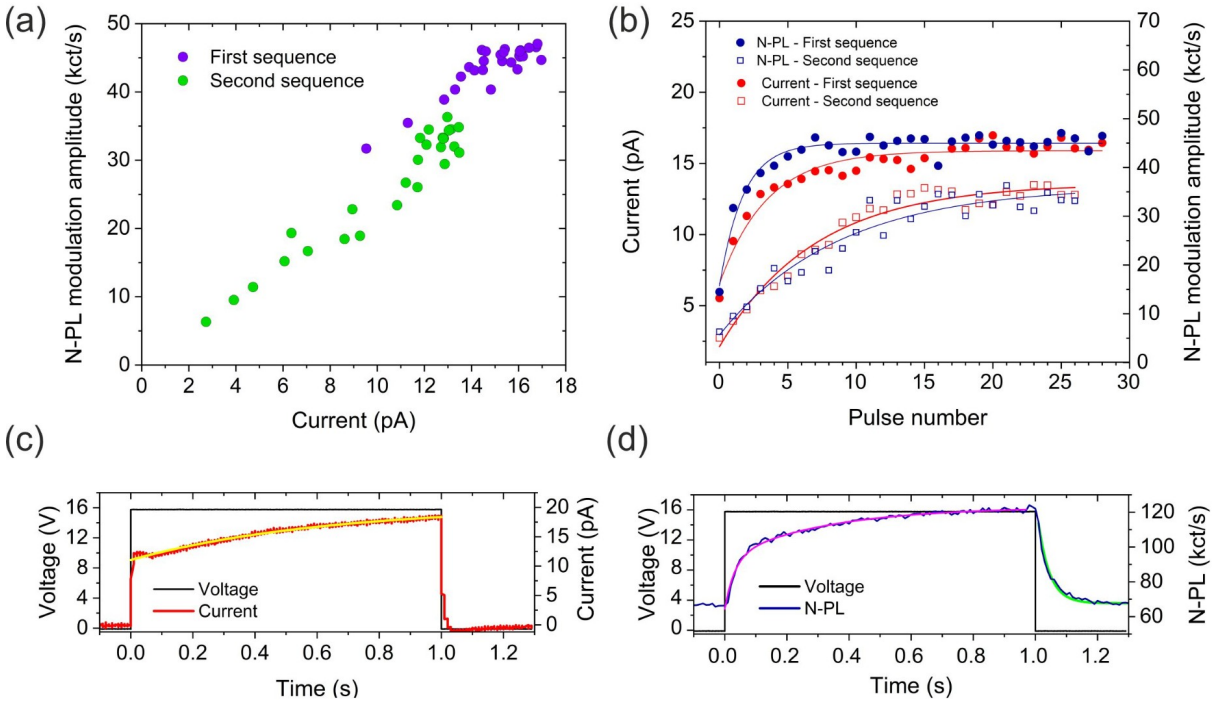

Figure 3: (a) Nonlinear photoluminescence (N-PL) modulation amplitude plotted against the electric current, I_g for the two positive bias sequences shown in Figure 2(c). (b) Pulse-to-pulse evolution of the N-PL modulation amplitude and I_g amplitude for the two positive bias sequences. Solid lines are fits of the data with a simple capacitor-like function. (c) and (d) I_g and N-PL intrapulse dynamics averaged over 29 consecutive positive bias pulses. A spurious 25 Hz component has been filtered out from the N-PL signal. I_g is fitted with a capacitor model in the slow-growth region to extract the time constant (yellow solid line). N-PL is best fitted with a double exponential after the leading bias edge (purple solid line). However, the decaying tail after the falling edge is well reproduced by as simple picture of a discharging capacitor (green solid line).

channels within the nanogap,[38,39] akin to typical memristive devices undergoing resistive changes.[40] Upon electrical stress, various processes are contributing to alter in time the SiO_2/PMMA environment composing the nanogap, including defect creation produced by electron injection (e.g., oxygen vacancies), Au ions diffusion, clustering and filamentary growth.[41–43] Indeed, PMMA has been successfully employed as a low-cost easily-processed organic material promoting filamentary-type resistive switching[44,45] whereby electrochemical reactions involving the migration and clustering metallic ions leads to the formation of an atomic conductive bridge across the gap.[40,46] Here, the current trace features a behavior mixing the occurrence of a non-volatile resistive state shown by the instantaneous rise of the current at the leading edge of the pulses, and an evolutionary nature materialized by a slow-growth response of hundreds of ms. The instantaneous rise of I_g preceding its growth is most probably linked to tunnel transport through the modified gap. A fit of the slow growth region using a simple model mimicking a diffusion capacitance (yellow line) yields a characteristic time of 490 ms. This time response of the current flow can be linked to the build-up of the conduction pathway in the nanogap under the influence of the applied electric field and is a strong indicator of a volatile memristive behavior.[47] Such progressive evolution of the transport have been previously experimentally observed in wide Au nanogaps fabricated on SiO_2 and were linked to the metallic diffusion and filament growth in the gap.[47,48] We confirm the presence of metal clusters in the nanogap with scanning electron imaging of similar devices operated in air (*i.e.* without the PMMA layer) and taken after extensive testing with positive and negative biases. Images are provided in Figure S3 within the Supporting Information. They clearly reveal deformed Au electrodes at the nanogap and the formation of nanometer-sized clusters, which were absent in the pre-activation SEM image. This confirms the role of field-driven surface modification on the N-PL baseline measured during the activation process of the system (Figure 2(b)).

Figure 3(d) shows the average N-PL dynamics during a pulse. Unlike the current, the enhancement of the emitted light is not instantaneous. A relatively fast raise is followed by

a slower progression. A double exponential fitting (purple curve) yields a fast exponent at 31 ms and a slower exponent at 330 ms, a latter value in line with the slow component of the current dynamics. The N-PL temporal trace shows the fast dynamics occurs also after the falling edge of the pulse. The N-PL decays to its baseline with a time constant of 36 ms, a value very close to the fast component measured at the onset of the bias pulse. Note that this decaying signal is not seen in the current trace after the bias returns to 0 V (Figure 3(c)). Within the 1 s pulse duration, the governing mechanism does not allow to reach a steady state amplitude of either of the two signals. This behavior is clear signature of the N-PL sensitivity to relaxation dynamics linked to a volatile resistive evolution and history of the nanogap. We provide in the following an interpretation how memristive dynamics may be governing the signal. Figure 4 presents three sketches illustrating the activated nanogap under three biasing conditions: when the AuNW is at a positive potential (a), neutral (b), and negative potential (c) with respect to the ground tapered Au electrode.

Positive bias pulse

When a positive bias pulse is applied to the AuNW (Figure 4(a)), the cathode is partially oxidized and generates Au ions while negatively charge defects injected in the nanogap during the activation phase counter-propagate along the electric field towards their respective counter-electrode. Migration of metal atoms/ions in the switching matrix follows multiple complex electrochemical processes and is driven by several factors such as material composition and applied field parameters.[49] An activation of pristine nanogaps with only one polarity (Figure S4 of the Supporting Information) confirms that Au atoms/ions are detached and are migrated along the electric field toward the counter electrode. For a positive bias, pre and post-activation SEM imaging reveals that a granular filament composed of nanoclusters has grown and the nanowire suffered from a reshaping of its extremity. This observation of electrode deformation and filament growth on counter electrode is in line with previous reports of Au/SiO2/Au systems.[47,48] In the present experiments, we did not apply

any compliance to the electric current. Hence, complete and stable filament formation is essentially inhibited due to destructive Joule heating of the conduction path as the electric current increases. Nonetheless, we have observed complete filament growth when a 1 GΩ resistance is placed in series with the nanogap to limit the maximum current running through the device. As shown in Figure S5 of Supporting Information, the current trace evolves to reach a stable switching pattern, characteristic of a fully non-volatile low resistive state and indicative of a metallic bridge formed between the contacts. The modulation of the N-PL maintained during the buildup phase washes out when the low resistive state occurs. In this situation, the applied potential is dropped at the series resistance. Charged species that may be present in the gap are no longer diffusing and the electron density at the surface of the AuNW remains unaffected by the bias. Consequently, the N-PL stays constant, as shown in Figure S5.

Coming back to the situation of a freely-evolving unprotected device, two factors likely contribute to the gradual increase of the N-PL during the pulse duration (Figure 3(d)): first, the electric field-driven volatile filamentary growth within the nanogap leads to a decrease in the effective size of the nanogap. For the same voltage applied, the electric field strength in the nanogap is thus stronger. This contributes to lowering the electron density at the surface of AuNW extremity and consequently to an enhancement of the N-PL, in agreement with our previous work.[31] The second contribution may stem from the increased density of mobile positive Au ions injected in the nanogap from the AuNW electrode during the voltage pulse. These positive metal ions near the metal surface give rise to a screened Coulomb potential and an effective lowering of the electron concentration. This may be the possible reason for the relatively slow rise of N-PL with a 31 ms time constant at the onset edge of the bias pulse compared to the current. Such tens of ms time scale are in the range of diffusion time of Ag clusters in.[50] Once the filament gets thicker the second effect is overtaken by the capacitive effect due to a smaller gap size.

Neutral potential between positive bias pulses

The effect of the volatile nature of the inclusions forming the conductive pathway on the N-PL manifests itself in the decaying tail of the signal after the falling edge of the voltage pulse (Figure 3(d)). When the electric field is no longer applied, metal ions freely diffuse and relax within a sub-second dynamics and presumably form nanoclusters in the dielectric matrix,[50,51] as illustrated in Figure 4(b). Freely diffusing Au ions may also be reduced at negatively charged sites. It is clear that the decaying tail of the N-PL signal is ruled by such complex relaxation kinetics of Au ions.

Negative bias pulse

Upon changing the polarity of the bias, diffusing species already present in the nanogap migrate in a reverse direction and leading to a dissolution of the conductive pathways previously built-up.[48] This is schematically pictured in Figure 4(c). The effective widening of the nanogap results in a presumably smaller capacitive effect on the electron concentration at the surface. This is confirmed by the absence of the expected N-PL reduction.[31] The dissolution of the conduction channel is corroborated by the much lower electrical current measured for the negative sequence in Figure 2(c), where the ON conductance (defined as the ratio of mean electric current during the bias pulses with the applied voltage) is 0.13 pS compared to 0.93 pS measured during the stable response under the initial positive pulses. The reversed bias polarity acts as a partial reset process.[52] However, because the memristor is composed of Au on both sides, filament growth in the reversed direction can be initiated by further increasing the negative bias applied to the AuNW. This situation is depicted in Figure S6, Supporting Information for $V = -20$ V. In this case, we clearly observe the expected quenching of the N-PL counts with negative bias pulses. These general results obtained on a single AuNW have been reproduced on multiple devices. While the measured modulation amplitudes vary between pulse sequences and between devices, they are repeatable, and we observe qualitatively the same behavior. To substantiate this claim, we show

in Figure S7, supporting information, N-PL modulation results for three additional AuNW systems embedded in air or PMMA switching matrices with varying gap sizes.

Investigating sub-pico Siemens conductance variation effect on N-PL modulation

In the following, we conduct a systematic examination of the modulation amplitude of the N-PL with varying conductance states of the nanogap under electrostatic driving. Our approach involves a control of the metallic filament growth through the application of sequences of electrostatic pulses. These pulses are maintained with a constant pulse width of $T_{\mathrm{ON}} = 100$ ms and a voltage amplitude of approximately +20 V. The control parameter is here interpulse delay, *i.e.* the duty cycle. Expressed as a percentage, the duty cycle δ represents the ratio of the pulse width (T_{ON}, fixed as 100 ms) to the period ($\mathrm{T_{period}}$) of the sequence as defined in Figure 5. For instance, $\delta = 2.5\%$ duty cycle allows the filament to undergo 100 ms of growth followed by a relaxation time of 3.9 s, enabling self-diffusion of the species contributing to the volatile conductive state. Conversely, a 50% duty cycle provides also 100 ms for growth but same for relaxation. The space accessible for the mobile species is therefore limited before the next pulse arrives. Hence, a smaller duty cycle leads to a lower conductive state compared to a larger duty cycle.

Figure 5(a) displays the time traces of the electric current and N-PL response across subsequent varying duty cycles. Clearly, the measurements confirm that the formation kinetics of the conduction path dictates the amplitude of both responses. The current level and enhancement of the N-PL remain modest for small duty cycles (i.e., longer relaxation times), but drastically increases when $\mathrm{T_{ON}}$ enables the memristive dynamics to occur. The luminescence baseline at $V = 0$ V remains fairly constant during this long time frame spanning over 400 s. Any drastic surface modification at the bias-controlled end of the AuNW would be seen as a fluctuating signal at $V = 0$ V, as in Figure 2(b). Detailed snapshots of the time series are visually presented in Figures 5(b) and (c) highlighting discernible differ-

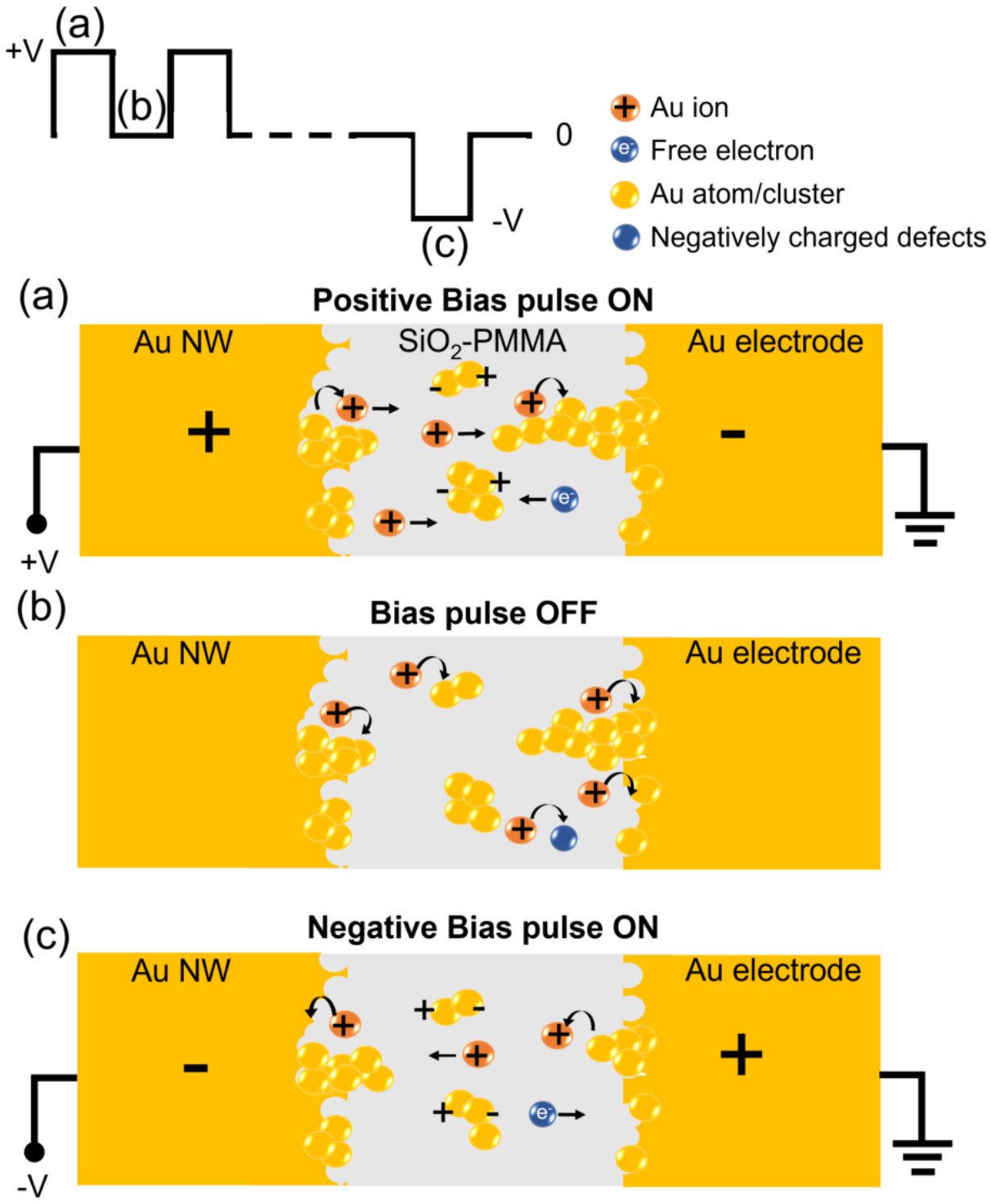

Figure 4: Schematic illustrations of positive Au atoms/ions and nanoclusters dynamics under (a) positive bias pulse, (b) between positive pulses (*i.e.*, no bias), and (c) negative bias pulse.

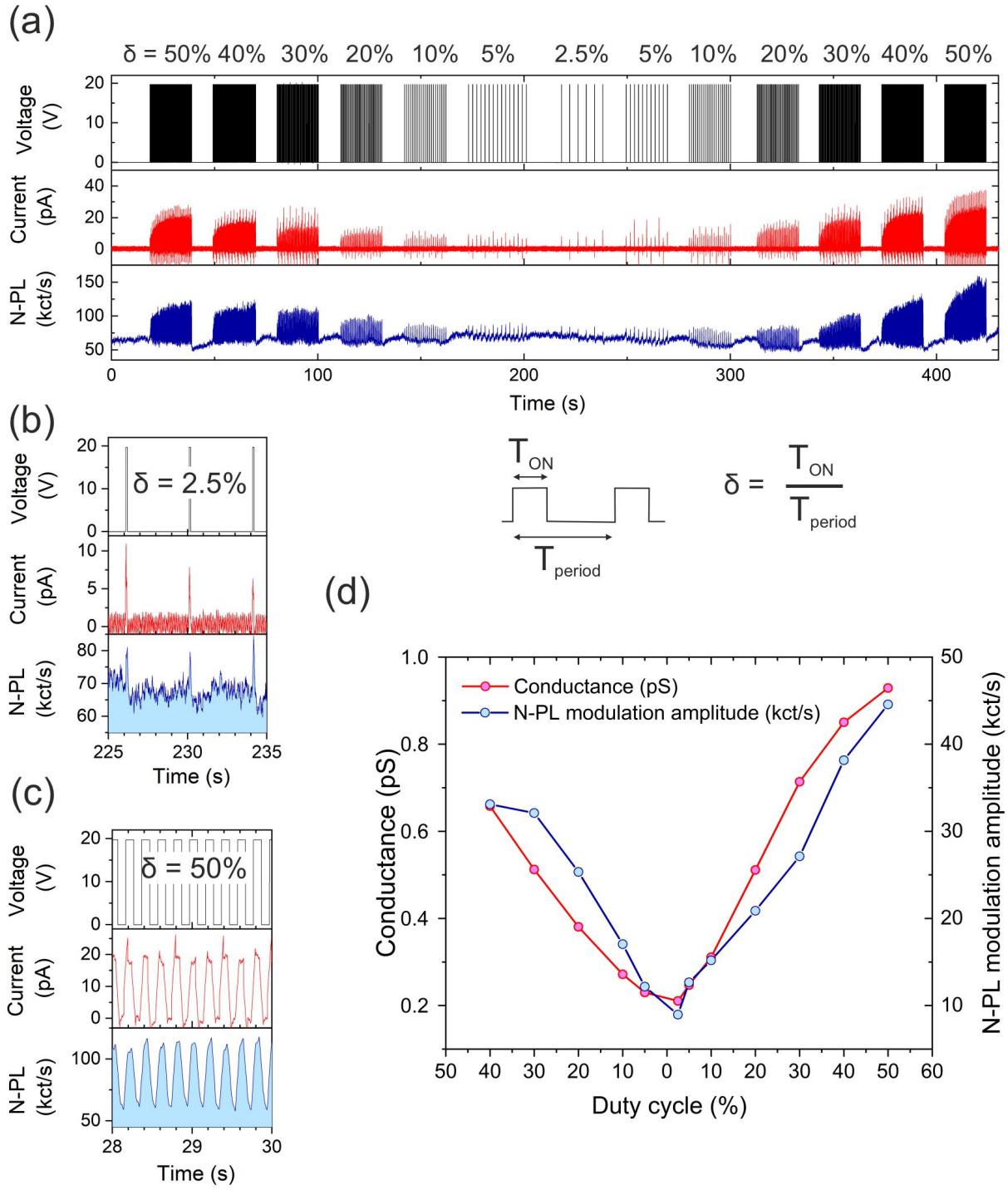

Figure 5: (a) Time series of nonlinear photoluminescence (N-PL) and electric current, I_g response under 100 ms bias pulse with +20 V amplitude and varying duty cycle $\delta = T_{ON}/T_{period}$ shown in the inset at the top. (b) and (c) Zoomed snapshots of time series for duty cycles $\delta = 2.5\%$ and $\delta = 50\%$. (d) N-PL modulation amplitude and average conductance of the nanogap during the bias pulse with varying duty cycles of applied bias pulses calculated from different bias pulse sequences of time series presented in (a).

ences in N-PL intensities and electric current for bias pulses with the extreme duty cycles. Figure 5(d) plots the N-PL modulation amplitude alongside the conductance (defined as the ratio of mean electric current during the bias pulse to the applied voltage) for varying duty cycles. Plotted values are averages across the sequences. Here too, the conductance and the N-PL modulation amplitudes are sharing the same dependence on the diffusive dynamics of the memristive gap. These findings systematically underscore the influence of sub-pico Siemens conductance variations resulting from bias-driven filament growth and relaxation on N-PL emitted from the extremity of the nanowire.

Conclusions

The past few years have witnessed a growing corpus of photonic memristors.[53,54] In this family of devices, absorption of light changes or facilitates resistive switching via different physical processes. Examples are photo-generated carriers modulating the device's conductance or the interface energy barrier, photo-induced phase transition in specific alloys, or photo-modification of the chemical composition.[55] Our approach with respect to this corpus takes a different stand by modifying an optical response by a memristive actuation. In summary, we presented a comprehensive experimental study of the influence of memristive dynamics on a plasmon-assisted nonlinear photoluminescence emitted by Au nanowire optically excited by focused ultrafast laser pulses. Local nonlinear photoluminescence measurements correlated with electric current flow show that field-induced dynamics leading to metallic filament formation and dissolution in the nanogap enables to modulate the intensity of the nonlinear surface response with a sub-pS sensitivity to conductance variations. These observations demonstrate that nonlinear photoluminescence can be a responsive probe for atomic scale dynamics ruling emerging memristive technologies. An important prospect of our work is the possibility to locally and electrically change the temperature of thermal electrons in an optically pumped system. We believe the system architecture explored in the

present work featuring electrically controlled remote sites will be an important platform to explore diverse applications where external controllability, agility and reconfigurability are required. They include electrically-tuned surface response of nanoscale resonators,[56] as well as controlled thermal management and supervision with non-uniform heat distributions.[57,58]

Methods

Device fabrication

The AuNW system was fabricated in two steps.[31] In the first step, we pattern smaller features of the system i.e., the nanowire and the tapered electrode forming a gap of tens of nanometers using e-beam lithography. A glass substrate was spin-coated with a double layer of Poly(methyl methacrylate) – PMMA with molecular weights of 50 kDa and 200 kDa (Allresist GmbH, ARP 639.04 and ARP 649.04) respectively followed by baking at 150°C temperature for both layers. Patterns are written with a dose of 420 $\mu C/cm^2$ at an acceleration voltage of 20 kV (Raith GmbH, Pioneer) and developed in developer ARP 600-56, Allresist GmbH for 40 s at room temperature. A 1 nm Cr layer followed by $\sim$ 90 nm Au layer is deposited using e-beam and thermal evaporation respectively in a vacuum chamber (Plassys, MEB400). Lift-off of the patterned substrate is performed in a remover (Allresist GmbH, ARP 600-71), followed by rinsing in deionized water and blow-drying with nitrogen. In the second step, microelectrodes connected to the nanowire and the tapered electrode are fabricated using photolithography. A photoresist (AZ nLOF, MicroChemicals GmbH) is spin-coated on already pattered nanostructures and baked at 110°C followed by microelectrodes patterning using MJB4 mask aligner, Süss GmbH. The resist is baked at 110°C post exposer and developed in the developer, AZ 826 MIF, MicroChemicals GmbH. Metal layers are deposited as in the first step followed by lift-off of the resist in a remover (Dow, 1165). Microelectrodes are wire-bonded to a PCB for external electrical control. AuNW systems are imaged using the scanning electron microscopy mode of Raith GmbH, Pioneer.

Association content

A preprint version of the manuscript is accessible via: Sharma, D. K.; Agreda, A.; DellOva, F.; Malchow, K.; Colas-des-Francs, G.; Dujardin, E.; Bouhelier, A. Memristive control of plasmon-mediated nonlinear photoluminescence in Au nanowires. 2024, arXiv, https://doi.org/10.48550/arXiv.2403.04581 (accessed March 7, 2024)

Supporting Information Available

The following files are available free of charge.

- Movie M1: Real-time visualization of the Nonlinear photoluminescence modulations under electrostatic bias pulses.
- Supporting information document: Electrical and optical characterization setup, Nonlinear photoluminescence spectrum, SEM images of nanogap for correlation study, Nonlinear photoluminescence modulation response for nanogap transitioning from high resistive state to conductive state, Time series of Nonlinear photoluminescence and electric current response with +20 V and -20 V bias pulse sequences, Nonlinear photoluminescence modulation from three additional AuNW systems embedded in air or PMMA switching matrices with varying nanogap sizes

Notes

The authors declare no competing financial interest.

Acknowledgement

This work has been partially funded by the French Agence Nationale de la Recherche (ANR-20-CE24-0001 DALHAI and ISITE-BFC ANR-15-IDEX-0003), the EIPHI Graduate School

(ANR-17-EURE-0002). Device fabrication and characterization were performed at the technological platforms ARCEN Carnot and SMARTLIGHT with the support of the French Agence Nationale de la Recherche under program Investment for the Future (ANR-21-ESRE-0040), the Région de Bourgogne Franche-Comté, the European Regional Development Fund (FEDER-FSE Bourgogne Franche-Comté 2021/2027), the CNRS and the French RENATECH+ network.

References

1. Haug, T.; Klemm, P.; Bange, S.; Lupton, J. M. Hot-Electron Intraband Luminescence from Single Hot Spots in Noble-Metal Nanoparticle Films. *Phys. Rev. Lett.* **2015**, *115*, 067403.

2. Saavedra, J.; Asenjo-Garcia, A.; García de Abajo, F. J. Hot-electron dynamics and thermalization in small metallic nanoparticles. *Acs Photonics* **2016**, *3*, 1637–1646.

3. Roloff, L.; Klemm, P.; Gronwald, I.; Huber, R.; Lupton, J. M.; Bange, S. Light emission from gold nanoparticles under ultrafast near-infrared excitation: Thermal radiation, inelastic light scattering, or multiphoton luminescence? *Nano letters* **2017**, *17*, 7914–7919.

4. Malchow, K.; Bouhelier, A. Photon bunching of the nonlinear photoluminescence emitted by plasmonics metals. *JOSA B* **2021**, *38*, 576–583.

5. Sivan, Y.; Un, I. W.; Kalyan, I.; Lin, K.-Q.; Lupton, J. M.; Bange, S. Crossover from Nonthermal to Thermal Photoluminescence from Metals Excited by Ultrashort Light Pulses. *ACS nano* **2023**,

6. Rodríguez Echarri, A.; Iyikanat, F.; Boroviks, S.; Mortensen, N. A.; Cox, J. D.; García de Abajo, F. J. Nonlinear Photoluminescence in Gold Thin Films. *ACS Photonics* **2023**, *10*, 2918–2929.

7. Demichel, O.; Petit, M.; Viarbitskaya, S.; Mejard, R.; de Fornel, F.; Hertz, E.; Billard, F.; Bouhelier, A.; Cluzel, B. Dynamics, efficiency, and energy distribution of nonlinear plasmon-assisted generation of hot carriers. *ACS Photonics* **2016**, *3*, 791–795.

8. Baida, H.; Mongin, D.; Christofilos, D.; Bachelier, G.; Crut, A.; Maioli, P.; Del Fatti, N.; Vallée, F. Ultrafast Nonlinear Optical Response of a Single Gold Nanorod near Its Surface Plasmon Resonance. *Phys. Rev. Lett.* **2011**, *107*, 057402.

9. Hou, X.; Djellali, N.; Palpant, B. Absorption of ultrashort laser pulses by plasmonic nanoparticles: not necessarily what you might think. *ACS photonics* **2018**, *5*, 3856–3863.

10. Suemoto, T.; Yamanaka, K.; Sugimoto, N.; Kobayashi, Y.; Otsu, T.; Tani, S.; Koyama, T. Relaxation dynamics of hot electrons in the transition metals Au, Ag, Cu, Pt, Pd, and Ni studied by ultrafast luminescence spectroscopy. *Journal of Applied Physics* **2021**, *130*.

11. Beversluis, M. R.; Bouhelier, A.; Novotny, L. Continuum generation from single gold nanostructures through near-field mediated intraband transitions. *Physical Review B* **2003**, *68*, 115433.

12. Imura, K.; Nagahara, T.; Okamoto, H. Near-field two-photon-induced photoluminescence from single gold nanorods and imaging of plasmon modes. *The Journal of Physical Chemistry B* **2005**, *109*, 13214–13220.

13. Ghenuche, P.; Cherukulappurath, S.; Taminiau, T. H.; van Hulst, N. F.; Quidant, R. Spectroscopic mode mapping of resonant plasmon nanoantennas. *Physical review letters* **2008**, *101*, 116805.

14. Gao, N.; Chen, Y.; Li, L.; Guan, Z.; Zhao, T.; Zhou, N.; Yuan, P.; Yao, S. Q.; Xu, Q.-H. Shape-dependent two-photon photoluminescence of single gold nanoparticles. *The Journal of Physical Chemistry C* **2014**, *118*, 13904–13911.

15. Wang, J.; Butet, J.; Baudrion, A.-L.; Horrer, A.; Lévêque, G.; Martin, O. J.; Meixner, A. J.; Fleischer, M.; Adam, P.-M.; Horneber, A., *et al.* Direct comparison of second harmonic generation and two-photon photoluminescence from single connected gold nanodimers. *The Journal of Physical Chemistry C* **2016**, *120*, 17699–17710.

16. Chen, J.; Krasavin, A.; Ginzburg, P.; Zayats, A. V.; Pullerits, T.; Karki, K. J. Evidence of high-order nonlinearities in supercontinuum white-light generation from a gold nanofilm. *ACS Photonics* **2018**, *5*, 1927–1932.

17. Großmann, S.; Friedrich, D.; Karolak, M.; Kullock, R.; Krauss, E.; Emmerling, M.; Sangiovanni, G.; Hecht, B. Nonclassical optical properties of mesoscopic gold. *Physical Review Letters* **2019**, *122*, 246802.

18. Dell'Ova, F.; Malchow, K.; Chassagnon, R.; Heintz, O.; Pocholle, N.; Colas des Francs, G.; Dujardin, E.; Bouhelier, A. Hot Carrier-Induced Nonlinear Photoluminescence in a Thin Indium Tin Oxide Layer Patterned by Ga Ion Beam Milling. *ACS Applied Optical Materials* **2023**, *1*, 244–251.

19. Bouhelier, A.; Bachelot, R.; Lerondel, G.; Kostcheev, S.; Royer, P.; Wiederrecht, G. P. Surface Plasmon Characteristics of Tunable Photoluminescence in Single Gold Nanorods. *Phys. Rev. Lett.* **2005**, *95*, 267405.

20. Muhlschlegel, P.; Eisler, H.-J.; Martin, O. J.; Hecht, B.; Pohl, D. Resonant optical antennas. *science* **2005**, *308*, 1607–1609.

21. Boyd, G. T.; Yu, Z. H.; Shen, Y. R. Photoinduced luminescence from the noble metals and its enhancement on roughened surfaces. *Phys. Rev. B* **1986**, *33*, 7923–7936.

22. Agreda, A.; Sharma, D. K.; Viarbitskaya, S.; Hernandez, R.; Cluzel, B.; Demichel, O.; Weeber, J.-C.; Colas des Francs, G.; Kumar, G. P.; Bouhelier, A. Spatial distribution of the nonlinear photoluminescence in au nanowires. *ACS photonics* **2019**, *6*, 1240–1247.

23. Viarbitskaya, S.; Demichel, O.; Cluzel, B.; Colas des Francs, G.; Bouhelier, A. Delocalization of Nonlinear Optical Responses in Plasmonic Nanoantennas. *Phys. Rev. Lett.* **2015**, *115*, 197401.

24. Wang, H.; Huff, T. B.; Zweifel, D. A.; He, W.; Low, P. S.; Wei, A.; Cheng, J.-X. In vitro and in vivo two-photon luminescence imaging of single gold nanorods. *Proceedings of the National Academy of Sciences* **2005**, *102*, 15752–15756.

25. Durr, N. J.; Larson, T.; Smith, D. K.; Korgel, B. A.; Sokolov, K.; Ben-Yakar, A. Two-photon luminescence imaging of cancer cells using molecularly targeted gold nanorods. *Nano letters* **2007**, *7*, 941–945.

26. Kumar, U.; Cuche, A.; Girard, C.; Viarbitskaya, S.; Dell'Ova, F.; Al Rafrafin, R.; Colas des Francs, G.; Bolisetty, S.; Mezzenga, R.; Bouhelier, A., *et al.* Interconnect-Free Multibit Arithmetic and Logic Unit in a Single Reconfigurable 3 μm2 Plasmonic Cavity. *ACS nano* **2021**, *15*, 13351–13359.

27. Zhang, Y.; He, S.; Guo, W.; Hu, Y.; Huang, J.; Mulcahy, J. R.; Wei, W. D. Surface-plasmon-driven hot electron photochemistry. *Chemical reviews* **2017**, *118*, 2927–2954.

28. Yang, J. J.; Strukov, D. B.; Stewart, D. R. Memristive devices for computing. *Nature Nanotechnology* **2013**, *8*, 13–24.

29. Lanza, M.; Sebastian, A.; Lu, W. D.; Le Gallo, M.; Chang, M.-F.; Akinwande, D.; Puglisi, F. M.; Alshareef, H. N.; Liu, M.; Roldan, J. B. Memristive technologies for data storage, computation, encryption, and radio-frequency communication. *Science* **2022**, *376*, eabj9979.

30. Thyagarajan, K.; Sokhoyan, R.; Zornberg, L.; Atwater, H. A. Millivolt modulation of plasmonic metasurface optical response via ionic conductance. *Advanced Materials* **2017**, *29*, 1701044.

31. Agreda, A.; Viarbitskaya, S.; Smetanin, I. V.; Uskov, A. V.; Colas des Francs, G.; Bouhelier, A. Electrostatic Control over Optically Pumped Hot Electrons in Optical Gap Antennas. *ACS photonics* **2020**, *7*, 2153–2162.

32. Song, M.; Dellinger, J.; Demichel, O.; Buret, M.; Des Francs, G. C.; Zhang, D.; Dujardin, E.; Bouhelier, A. Selective excitation of surface plasmon modes propagating in Ag nanowires. *Optics express* **2017**, *25*, 9138–9149.

33. Weeber, J.-C.; Dereux, A.; Girard, C.; Krenn, J. R.; Goudonnet, J.-P. Plasmon polaritons of metallic nanowires for controlling submicron propagation of light. *Physical Review B* **1999**, *60*, 9061.

34. Zhu, Y.; Cui, L.; Natelson, D. Hot-carrier enhanced light emission: The origin of above-threshold photons from electrically driven plasmonic tunnel junctions. *J. Appl. Phys.* **2020**, *128*, 233105.

35. Berthelot, J.; Bachelier, G.; Song, M.; Rai, P.; Colas des Francs, G.; Dereux, A.; Bouhelier, A. Silencing and enhancement of second-harmonic generation in optical gap antennas. *Opt. Express* **2012**, *20*, 10498–10508.

36. Mennemanteuil, M.-M.; Dellinger, J.; Buret, M.; Colas-des-Francs, G.; Bouhelier, A. Pre-determining the location of electromigrated gaps by nonlinear optical imaging. *Appl. Phys. Lett.* **2014**, *105*, 021101.

37. Agreda, A.; Sharma, D. K.; Des Francs, G. C.; Kumar, G. P.; Bouhelier, A. Modal and wavelength conversions in plasmonic nanowires. *Optics Express* **2021**, *29*, 15366–15381.

38. Mehonic, A.; Cueff, S.; Wojdak, M.; Hudziak, S.; Jambois, O.; Labbé, C.; Garrido, B.; Rizk, R.; Kenyon, A. J. Resistive switching in silicon suboxide films. *Journal of Applied Physics* **2012**, *111*.

39. Menzel, S.; Waser, R. *Advances in Non-Volatile Memory and Storage Technology*; Elsevier, 2019; pp 137–170.

40. Yang, Y.; Gao, P.; Gaba, S.; Chang, T.; Pan, X.; Lu, W. Observation of conducting filament growth in nanoscale resistive memories. *Nature communications* **2012**, *3*, 732.

41. Lombardo, S.; Stathis, J. H.; Linder, B. P.; Pey, K. L.; Palumbo, F.; Tung, C. H. Dielectric breakdown mechanisms in gate oxides. *Journal of applied physics* **2005**, *98*.

42. Yang, J. J.; Pickett, M. D.; Li, X.; Ohlberg, D. A. A.; Stewart, D. R.; Williams, R. S. Memristive switching mechanism for metal/oxide/metal nanodevices. *Nature Nanotechnology* **2008**, *3*, 429–433.

43. Yang, Y.; Gao, P.; Gaba, S.; Chang, T.; Pan, X.; Lu, W. Observation of conducting filament growth in nanoscale resistive memories. *Nature communications* **2012**, *3*, 732.

44. Wolf, C.; Nau, S.; Sax, S.; Busby, Y.; Pireaux, J.-J.; List-Kratochvil, E. J. W. Resistive switching based on filaments in metal/PMMA/metal thin film devices. *Jpn. J. Appl. Phys.* **2015**, *54*, 120301.

45. Mangalam, J.; Agarwal, S.; Resmi, A.; Sundararajan, M.; Jinesh, K. Resistive switching in polymethyl methacrylate thin films. *Organic Electronics* **2016**, *29*, 33–38.

46. Sun, W.; Gao, B.; Chi, M.; Xia, Q.; Yang, J. J.; Qian, H.; Wu, H. Understanding memristive switching via in situ characterization and device modeling. *Nature communications* **2019**, *10*, 3453.

47. Sakai, K.; Sato, T.; Tani, S.; Ito, M.; Yagi, M.; Shirakashi, J.-I. Synaptic behaviors of electromigrated Au nanogaps. *AIP Advances* **2019**, *9*.

48. Sakai, K.; Sato, T.; Kiyokawa, R.; Koyama, R.; Yagi, M.; Ito, M.; Shirakashi, J.-I. Gold nanogap-based artificial synapses. *Japanese Journal of Applied Physics* **2020**, *59*, 050601.

49. Yang, Y.; Gao, P.; Li, L.; Pan, X.; Tappertzhofen, S.; Choi, S.; Waser, R.; Valov, I.; Lu, W. D. Electrochemical dynamics of nanoscale metallic inclusions in dielectrics. *Nature communications* **2014**, *5*, 4232.

50. Wang, Z.; Joshi, S.; Savel'ev, S. E.; Jiang, H.; Midya, R.; Lin, P.; Hu, M.; Ge, N.; Strachan, J. P.; Li, Z., *et al.* Memristors with diffusive dynamics as synaptic emulators for neuromorphic computing. *Nature materials* **2017**, *16*, 101–108.

51. Cheng, B.; Zellweger, T.; Malchow, K.; Zhang, X.; Lewerenz, M.; Passerini, E.; Aeschlimann, J.; Koch, U.; Luisier, M.; Emboras, A., *et al.* Atomic scale memristive photon source. *Light: Science & Applications* **2022**, *11*, 78.

52. Mohammad, B.; Jaoude, M. A.; Kumar, V.; Homouz, D. M. A.; Nahla, H. A.; Al-Qutayri, M.; Christoforou, N. State of the art of metal oxide memristor devices. *Nanotechnology Reviews* **2016**, *5*, 311–329.

53. Martino, G. D.; Tappertzhofen, S. Optically accessible memristive devices. *Nanophotonics* **2019**, *8*, 1579–1589.

54. Youngblood, N.; Ocampo, C. A. R.; Pernice, W. H. P.; Bhaskaran, H. Integrated optical memristors. *Nature Phot.* **2023**, *17*, 561–572.

55. Wang, W.; Gao, S.; Wang, Y.; Li, Y.; Yue, W.; Niu, H.; Yin, F.; Guo, Y.; Shen, G. Advances in Emerging Photonic Memristive and Memristive-Like Devices. *Advanced Science* **2022**, *9*, 2105577.

56. Zurak, L.; Wolff, C.; Meier, J.; Kullock, R.; Mortensen, N. A.; Hecht, B.; Feichtner, T. Direct electrical modulation of surface response in a single plasmonic nanoresonator. *arXiv preprint arXiv:2307.01423 (accessed 4 July 2023)*

57. Lyu, P.-T.; Liu, X.-R.; Yin, L.-X.; Wu, P.; Sun, C.; Chen, H.-Y.; Xu, J.-J.; Kang, B.

Periodic Distributions and Ultrafast Dynamics of Hot Electrons in Plasmonic Resonators. *Nano Letters* **2023**, *23*, 2269–2276.

58. Bryche, J.-F.; Vega, M.; Moreau, J.; Karsenti, P.-L.; Bresson, P.; Besbes, M.; Gogol, P.; Morris, D.; Charette, P. G.; Canva, M. Ultrafast Heat Transfer at the Nanoscale: Controlling Heat Anisotropy. *ACS Photonics* **2023**, *10*, 1177–1186.

TOC Graphic

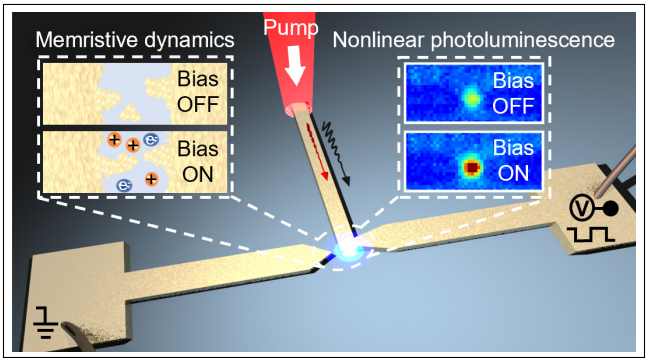
Memristive dynamics
Bias OFF
Bias ON
Pump
Nonlinear photoluminescence
Bias OFF
Bias ON